

# Structural design and analysis of micromachined ring-type vibrating sensor of both yaw rate and linear acceleration

Jui-Hong Weng<sup>a,1,2</sup>, Wei-Hua Chieng<sup>a,\*</sup>, Jenn-Min Lai<sup>b,2</sup>

<sup>a</sup> Department of Mechanical Engineering, National Chiao Tung University, 1001 Ta Hsueh Rd, Hsinchu Taiwan, ROC

<sup>b</sup> R&D Center, NeoStones MicroFabrication Corporation, 10F, No. 1, Li-Hsin 5th Road, SBIP, Hsin-chu, Taiwan, ROC

Received 10 March 2004; received in revised form 1 June 2004; accepted 17 June 2004

Available online 27 July 2004

## Abstract

This work presents the design and analysis of a micromachined ring-type motion sensor which can sense both the yaw rate and linear acceleration of a device in that it is installed. It integrates the functions of a gyroscope and an accelerometer. The design of the microstructure is based on the structure of a vibrating ring gyroscope. The analysis, considering the symmetry of the structure, implies that the rotational symmetry and mirror symmetry of the microstructure markedly affect the performance of the sensor. The modes of vibration determined using finite element analysis and the theoretical calculation of the resonant frequency of the structure are presented. The sensitivities of the characteristic of the sensor to the design specification, the fabrication errors and the theoretical errors are discussed. The structure is fabricated based on deep silicon etching and wafer bonding techniques. The process is developed for eliminating the aspect ratio dependent effect (ARDE) in dry etching process.

© 2004 Elsevier B.V. All rights reserved.

**Keywords:** Gyroscope; Accelerometer; Symmetry; MEMS

## 1. Introduction

Sensors for detecting motion have received considerable interest in recent decades. The gyroscope and the accelerometer represent two important categories of inertial technology for detecting motion. Sensor technology has evolved from discrete, expensive and inflexible units to smart, self-calibrating, silicon-based devices, which are integrated, low-cost and small, and exhibits other advantageous properties [1]. The rapid development of semiconductor technology has enabled micro electromechanical systems (MEMS), including micromachined gyroscopes and accelerometers, to keep up with the requirements of modern sensors. The gyroscope is

used in many applications, including guidance systems, navigation systems and control systems. Specific applications of the gyroscope include tactical weapon guidance, ship and airplane navigation, craft attitude control, motor sensors and commercial electronics.

Many important ideas related to gyroscope have been successfully developed. The conventional gimbaled spinning wheel or rotor is the most well known gyroscope. The laser ring gyro is also extensively applied and has been proven to be successful in inertial navigation applications [2]. Although highly accurate, these devices are too expensive for low-cost applications and too large to meet requirements of minimal size. The vibrating gyroscope is another successful class of gyro designs. It uses vibrating mechanical elements to sense rotation, and so requires no spinning or lubricated parts. In the 1960s, engineers tried to use vibrating elements, rather than rotating bodies, to sense the Coriolis force. Most gyroscope engineers developed vibrating gyroscopes based on vibrating strings and tuning forks. The use of vibrating gyroscopes not only keeps down the cost of devices but also

\* Corresponding author. Tel.: +886 3 5712121x55152; fax: +886 3 5720634.

E-mail address: [whc@cc.nctu.edu.tw](mailto:whc@cc.nctu.edu.tw) (W.-H. Chieng).

<sup>1</sup> Tel: +886 3 5712121x55170, fax: +886 3 5731754.

E-mail address: [juihongweng.me87g@nctu.edu.tw](mailto:juihongweng.me87g@nctu.edu.tw).

<sup>2</sup> Tel: +886 3 5712121x55170, fax: +886 3 5731754.

E-mail address: [a1005@neostones.com.tw](mailto:a1005@neostones.com.tw).

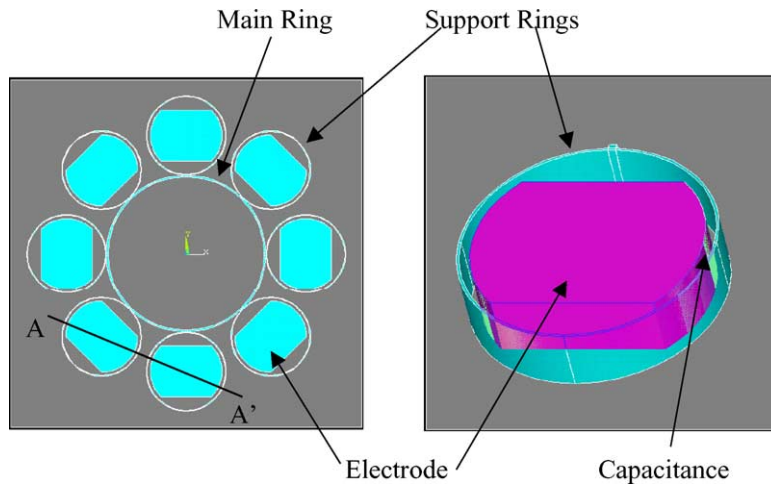


Fig. 1. Top and detailed views of structure that includes electrodes.

maintains performance because they can be manufactured precisely. The vibrating string gyro, the tuning fork gyro and the vibrating shell gyro are known as vibratory rate sensors or rotation sensors [2]. All can be implemented with micro-machining technology, and many designs have been carried out [3–18]. The hemispherical resonator gyroscope (HRG) [19], a vibrating shell gyro, has achieved inertial navigation performance levels that rival those of the laser ring gyro. The vibrating ring-type gyro, which is a simplified case of the vibrating shell gyro, is the subject of this work. The specific structural design of such gyro makes it particularly candidates for integration into accelerometers.

The accelerometer has been used in many engineering applications over several decades and many successful designs exist. Since Roylance developed the piezo-resistive silicon accelerometer [20] in 1977, the silicon-based accelerometer has become a mainstream detector of acceleration, replacing the convectional pendulous accelerometer. Such silicon-based devices can be classified into piezo-resistive, capacitive, piezo-electric, junction-effected, thermal, elec-

tromagnetic and electron tunneling accelerometers [21–26]. Its structural design and simplicity of fabrication make the capacitive accelerometer a popular type of accelerometer. Furthermore, the basic scheme of the capacitive accelerometer exploits electrostatic force, which can drive a vibrating microstructure.

Notably, the vibration of a circular ring can be theoretically decoupled into several modes. The first mode stands for the linear motion, and the second involves rotation. Two independent vibration modes exist concurrently. Therefore, the capacitive accelerometer and the vibrating ring gyroscope can be integrated in a motion sensor that detects both acceleration and rotation.

## 2. Sensor structure and control loops

The sensor design comprises the structure and the control loops. Fig. 1 presents the top and detailed views of the structure of the sensor. The main ring in the center is the main

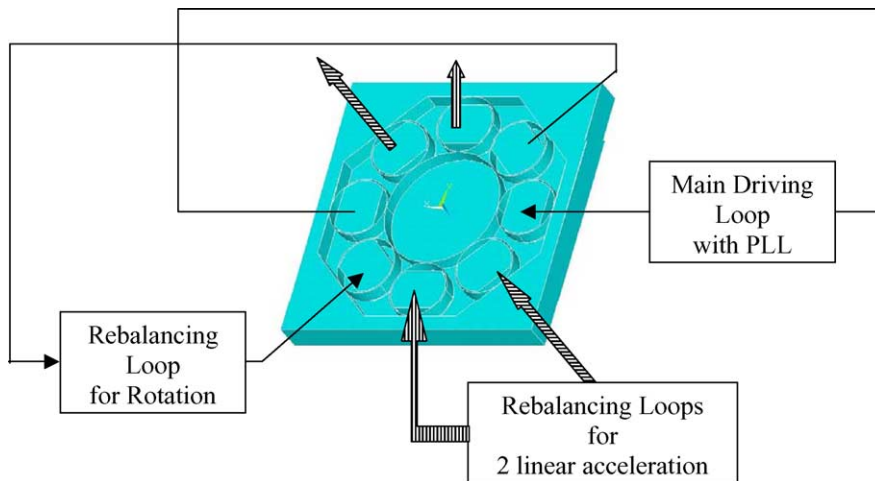


Fig. 2. Schematic overview of control loops and structure.

body designed to vibrate in the flexural mode. Fig. 2 indicates how the main ring is connected to eight support rings that surround it. The similarity between the shape of the main ring and that of the support rings simplifies the analysis. The main ring and the support rings are designed to vibrate in the plane, as depicted in Fig. 7. Electrodes are located at the centers of the support rings, as shown in Fig. 1, forming capacitors and driving the structure. The potential difference between the support ring and the electrode generates an electrostatic force that attracts them toward each other, and drives the structure to vibrate. The electrodes are shaped to maximize effective displacement when the structure vibrates in the desired modes of vibration.

Fig. 2 schematically depicts the control loops that are used to manipulate the sensor. The main driving loop causes the structure to vibrate as desired. The vibration is enhanced by phase-locked loops, and the structure vibrates at the resonant frequency to yield large amplitudes [27]. A rebalancing loop is designed to rebalance the vibration induced by the Coriolis force. Two rebalancing loops are designed to balance the vibration induced by linear motion. Three rebalancing loops cooperate to balance the planar motion.

### 3. Governing equation of the vibrating ring

Fig. 3 depicts the coordinate system of the motion sensor, including the inertial coordinate, the translating and rotating coordinate and the sensor coordinate. The sensor translates, without rotation, relative to a translating and rotating frame, which moves relative to a fixed inertial coordinate, where  $\vec{r}_1$  specifies the position vector from inertial coordinate to the translating and rotating coordinate and  $\vec{r}_2$  specifies the position vector from the frame to the sensor. The sensor is taken as a vibrating ring with a radius of  $r_3$ . The vibration of the main ring is considered to include radial and tangential displacements, denoted as  $u$  and  $v$ , respectively. Assume that the elongation of the central line of the ring remains constant in the flexural mode. The radial and tangential displacements

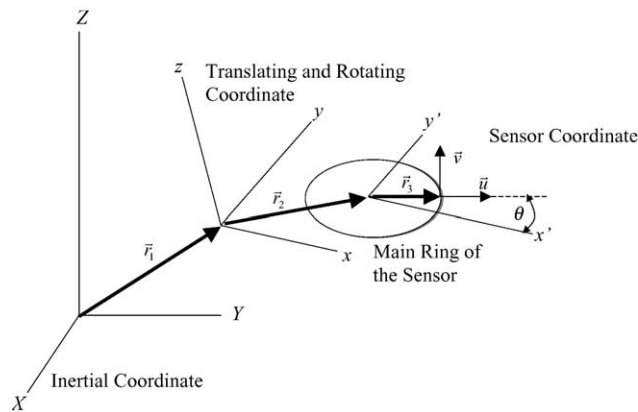


Fig. 3. Coordinate system of the sensor.

are,

$$\begin{aligned} u &= \sum (a_n \cos n\theta + b_n \sin n\theta) \\ v &= \sum \left( -\frac{a_n}{n} \sin n\theta + \frac{b_n}{n} \cos n\theta \right), \end{aligned} \quad (1)$$

where  $a$  and  $b$  are functions of time, and  $n$  denotes the number of modes [28]. These terms,  $\cos n\theta$  and  $\sin n\theta$ , are orthogonal on the interval  $0 \leq \theta \leq 2\pi$ . The designed structure is a complete ring, such that one time function is independent of the others.

To simplify the derivation,  $r_1$  is omitted and the position of the ring is expressed as,

$$X = \vec{r}_2 + \vec{r}_3 + \vec{u} + \vec{v}, \quad (2)$$

and the velocity  $V$  of the sensor is expressed as,

$$V = \frac{d}{dt}(X) + \Omega X, \quad (3)$$

where  $\Omega$  is the rate of rotation of the frame. The kinetic energy and potential energy of the ring are,

$$\begin{aligned} T &= \frac{1}{2} \rho t w r_3 \int_0^{2\pi} V \cdot V d\theta \\ U &= \frac{EI}{2r_3^3} \int_0^{2\pi} \left( \frac{\partial^2 u}{\partial \theta^2} + u \right)^2 d\theta \end{aligned} \quad (4)$$

where  $\rho$  is ring's density;  $t$  the ring's thickness;  $w$  the ring's width;  $E$  the Young's modulus of the material, and  $I$  its moment of inertia. Lagrange's equation, taking  $a_2$  as a generalized coordinates yields the differential equation of motion,

$$\begin{aligned} \frac{5}{8} m \ddot{a}_2 - m \Omega_z \dot{b}_2 - \frac{1}{2} m \dot{\Omega}_z b_2 \\ + \frac{9\pi EI}{r_3^3} a_2 + \left( \frac{5}{16} m a_2 \Omega_x^2 - \frac{5}{16} m a_2 \Omega_y^2 - \frac{5}{8} m a_2 \Omega_z^2 \right) \\ + \left( \frac{3}{8} m r_3 \Omega_x^2 - \frac{3}{8} m r_3 \Omega_y^2 \right) = f_{a_2}. \end{aligned} \quad (5)$$

This equation governs the second mode of flexural vibration of the ring, as depicted in Fig. 4. The detection of rotation depends on the second mode. This expression involves the centrifugal force associated with  $a_2$  and  $r_3$ . In this work, these terms are made relatively small by designing the structure with a high effective stiffness, which affects the flexural vibration. Besides, those terms associated with  $r_3$  will not appear in the higher order vibrations, such as the third mode. A higher order vibration may be a solution when a low stiffness and a large radius are required.

Fig. 5(a) indicates the second mode of vibrations of the ring, including the primary mode and secondary mode. The modes are mutually independent, and spatially orthogonal. Fig. 5(b) shows the ring that vibrates along the  $0^\circ$  axis. The ring is simply divided into four sectors, and there is an equivalent velocity representing the velocity of each sector. When the ring is rotated, the Coriolis force is induced and the resultant force lies along the  $45^\circ$  axis, as indicated in Fig. 5(c). Hence, the Coriolis force generates the secondary mode of vibration.

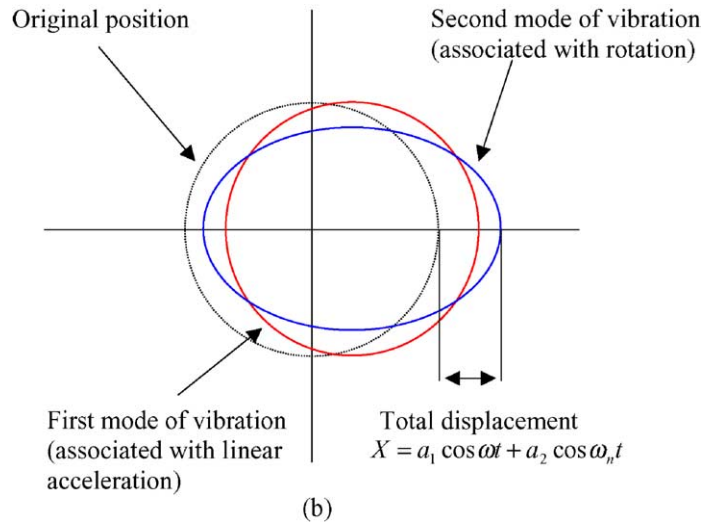


Fig. 4. Motion of the ring, comprising first and second modes of vibration.

Considering Eq. (4), using *Lagrange's equation*, and taking  $a_1$  as the generalized coordinate, yield the differential equation of motion is expressed as,

$$m\ddot{a}_1 - (2m\Omega_z \dot{b}_1 + mb_1 \dot{\Omega}_z) + (m\Omega_x \Omega_y b_1 - ma_1 \Omega_z^2 - ma_1 \Omega_y^2) + m\ddot{x} - (2m\Omega_z \dot{y} + my \dot{\Omega}_z - 2m\Omega_y \dot{z} - mz \dot{\Omega}_y) + (mz \Omega_x \Omega_z + my \Omega_x \Omega_y - mx \Omega_y^2 - mx \Omega_z^2) = f_{a_1}, \quad (6)$$

where  $x$ ,  $y$  and  $z$  are relative position vectors of the sensor in the translating and rotating frame, and  $a_1$  and  $b_1$  represent the rigid body motion of the ring. This equation governs the first mode of flexural vibration of the ring, as depicted in Fig. 4. The detection of linear acceleration depends on the first mode. In the first row of Eq. (6), the centrifugal terms are smaller than other terms on micro scale. The last two rows in Eq. (6) represent the rigid body motion of the sensor. They can be shifted to the right of the equation and considered as part of the applied force, such that the applied force is a function of position. The force is comparable to other terms in the governing equation and may pull the structure far away from its linear region. Hence, the rebalancing loop must be used.

#### 4. Symmetry of structure

The structural design of the motion sensor is determined with reference to both rotation and acceleration. The structure consists of the main ring and the supports. The influence of the symmetry on the support is discussed.

The first consideration in designing the support is the function of a gyroscope. The main ring surrounded by four asymmetric supports, as shown in Fig. 6(a), is the simplest arrangement for the gyroscopic function. Those supports are placed in directions  $a_2$  and  $b_2$ , such that the structure is equally stiff in these directions. However, two of the second modes of vibration of the structure are not exactly at  $45^\circ$  to each other and their natural frequencies are different. The structure exhibits planar motion when it vibrates, causing extra energy to be lost. The deformation of the support is not uniform, generating noise that affects detection. Thus, the supports should be placed as presented in Fig. 6(b), with rotational symmetry denoted by  $C_8$  [29]. This arrangement yields a balanced device with two modes that have the same natural frequency [30] at  $45^\circ$  to each other.

The centrifugal force and Coriolis force are generally applied simultaneously. The performance of a gyroscope under

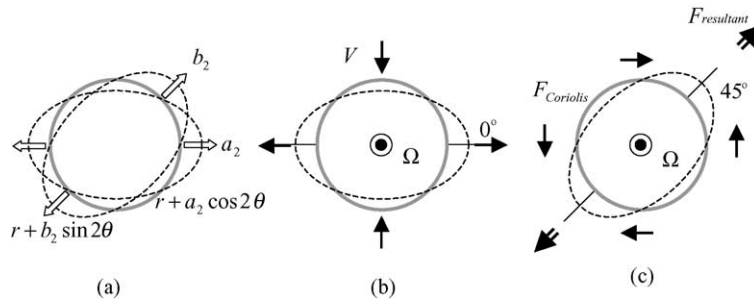


Fig. 5. (a) Second mode of vibration and its generalized coordinates; (b) primary mode on  $0^\circ$  axis; and (c) the secondary mode and resultant Coriolis force on  $45^\circ$  axis.

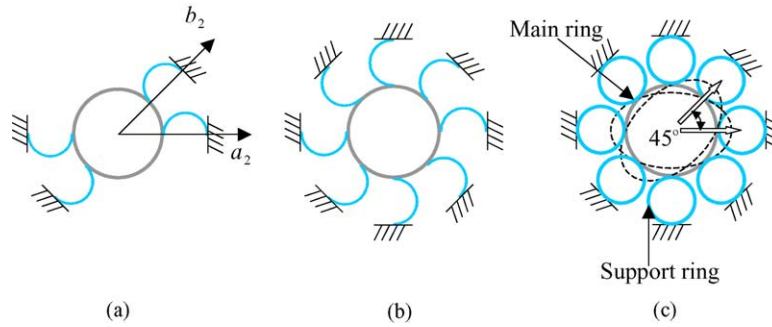


Fig. 6. Arrangements of supports: (a) four supports; (b) eight asymmetric supports; and (c) eight symmetric supports.

acceleration must be considered. When those structures illustrated in Fig. 6(a) and (b) are exposed to accelerations, main rings become deformed. The acceleration induces non-collinear displacement, which generates detected noise. The asymmetry of the supports is responsible for these defects. A feedback control loop may be used to rebalance those phenomena, but the design of control loops is complicated. Fortunately, those effects are not very serious on the micro scale, yet they cause undesired noise. Besides, asymmetric supports induce much more stress on the connection between the main ring and the supports.

A higher degree of symmetry of the structure presents better performance. Fig. 6(c) depicts the structure that contains symmetric supports. The structure is both mirrors symmetric and rotationally symmetric, and the degree of symmetry is denoted as  $D_4$ . The shape of the support is the same as that of the main ring, simplifying the estimation of the dynamic response. As expected, two modes are  $45^\circ$  to each other as shown in Fig. 7(a) and (b). This structure exhibits a collinear force–displacement relationship, and is insensitive to those defects described above. The mirror symmetry of the structure facilitates the design of the rebalance loops that compensate for accelerations. The compensating voltage is proportional to the acceleration, so the structure can be used as an accelerometer. The symmetry of the structure, on which the use of the sensor as a gyroscope and accelerometer depends, is both rotational and mirrors symmetry.

**5. Scheme for detecting rotation and acceleration**

When both the main ring and support rings of the sensor are considered, the governing equation of the  $n$ th mode vibration is represented as follows.

$$\begin{cases} A\ddot{a}_n - B\Omega\dot{b}_n - B_2\dot{\Omega}b_n + c\dot{a}_n + Ca_n = F_{a_n} \\ A\ddot{b}_n + B\Omega\dot{a}_n + B_2\dot{\Omega}a_n + c\dot{b}_n + Cb_n = F_{b_n} \end{cases}, \quad (7)$$

where  $A$  is the effective mass;  $B$  and  $B_2$  are the effective masses associated with the Coriolis force;  $c$  is the effective damping;  $C$  is the effective stiffness;  $F_{a_n}$  and  $F_{b_n}$  are the generalized forces, and  $\ddot{a}_n$  and  $\ddot{b}_n$  are generalized coordinates of the  $n$ th mode of vibration.

This work addresses the first and second modes. The first mode involves linear acceleration, and the second involves rotation. Fig. 4 indicates the motion of the ring consists of the first and second modes of vibration. Fig. 2 implies that the second mode of vibration is driven by the main driving loop. The rebalancing loop for detection is added to sense the rotation without which the signal process would be much more complex. Based on Eq. (7), with reference to the second mode but ignoring the angular acceleration, the driving forces are as follows.

$$\begin{aligned} F_{a_2} &= \sin \omega t \\ F_{b_2} &= -Kb_2' \end{aligned} \quad (8)$$

where  $\omega$  is the natural frequency of the second mode and equals  $\sqrt{C/A}$  and  $K$  is gain of the rebalancing force which is exerted by the rebalancing loop. The output signal determined

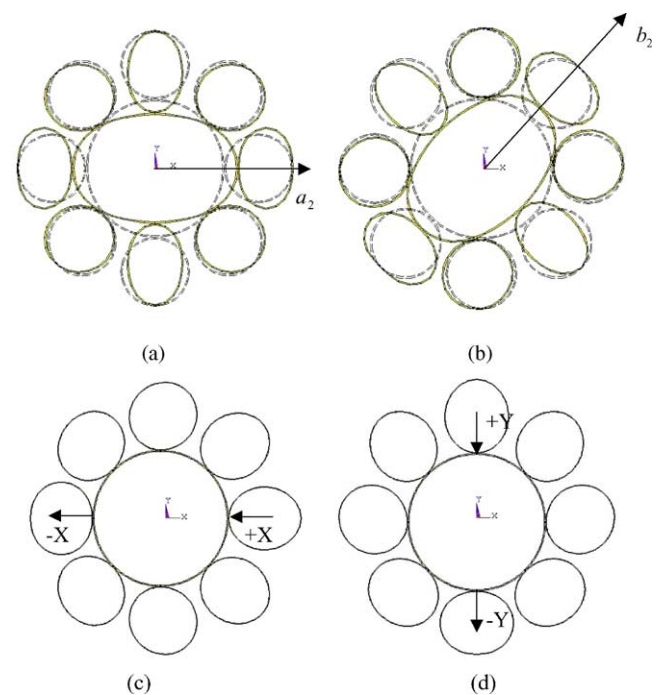
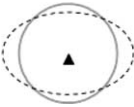
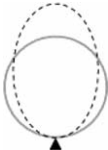
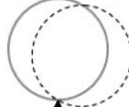


Fig. 7. (a and b) Scheme for detecting rotation of gyroscope; (c and d) scheme for detecting linear acceleration of accelerometer.

Table 1  
Natural frequency of separated parts of the structure

	Main ring	Extending support ring	Rotating support ring
Mode			
Natural frequency	$\omega_1 = \sqrt{\frac{3}{5} \frac{E}{\rho} \frac{w^2}{r^4}}$	$\omega_2 = 1.24\omega_1$	$\omega_3 = 0.4\omega_1, \omega'_3 = 2.58\omega_1$

by the rebalancing loop is,

$$V_{rot} = Kb_2 = -\Omega \frac{B}{c} \sin \omega t. \tag{9}$$

The output voltage is proportional to the rate of rotation. This finding is obtained by setting a large gain of rebalancing force, making  $b_2$  much smaller than  $a_2$  in Eq. (7), such that the terms in  $b_2$  can be neglected. Fig. 7(a) and (b) depict the detection scheme used to measure the rate of rotation. The fixed amplitude of the primary mode is driven in  $a_2$  and the Coriolis force induces a response in the form of the secondary mode in  $b_2$ .

As shown in Fig. 2, the first mode of vibration is rebalanced by two rebalancing loops to sense linear accelerations. The amplitude of induced displacement is constrained by the applied force, the driving frequency, effective stiffness, and gain of the rebalancing force. When the driving frequency is much smaller than the resonant frequency of the first mode, the amplitude is approximated to,

$$\frac{f}{C + K}. \tag{10}$$

The effective stiffness is designed to be high to reduce the amplitude as much as possible. Also, the rebalance loop is added to yield the readout circuit. Fig. 7(c) and (d) present the detection scheme for sensing acceleration. The opposing support rings are displaced equally when the structure is accelerated. The difference between the induced signals of the displacements of the opposing support rings represents the acceleration.

### 6. Natural frequency

Many microstructures vibrate at natural frequencies with large amplitude, as does the sensor proposed herein. The calculation of the natural frequency is important, because the frequency relates to the working point of the circuit of the sensor. The readout circuit is designed to suit this frequency, which also affects the performance of the sensor. Designing the circuit with an excessively high frequency raises many problems, such as the band limitation of an operational amplifier.

The process of estimating the natural frequency is separating the structure into three parts; determining the natural frequency of each part individually, and then calculating the composite natural frequency of the structure. The structure is separated into the main ring, extending support rings and rotating support rings. The similarity between the main ring and the supports simplifies the calculation. Table 1 lists the mode and natural frequency of separated parts of the structure.

Problematically, the natural frequency of the rotating support ring is not close to  $\omega_1$ . Accordingly, the frequencies of the two modes close to  $\omega_1$ , with the same boundary conditions, are estimated. The exact frequency is determined using two concepts. The first is to weight the effective mass. The mode of vibration of a composite structure should be similar to that of a substructure with a greater effective mass. In the design proposed here, the effective mass of the main ring is weighted more heavily and the mode of the structure is close to that of the main ring. The extending support rings are also heavily weighted. Hence, the natural frequency of the structure should be between  $\omega_1$  and  $\omega_2$ . The second concept is the impedance for each mode. The impedance of a mass-spring

Table 2  
Comparison of calculated and simulated results

	Analytical	FEM (Ansys5.3)
Resonant frequency of center fixed ring (Hz)	20926	20990
Resonant frequency of side fixed extension ring (Hz)	25955	25457
Resonant frequency of side fixed rotation ring (Hz)	8456	9047
Resonant frequency of total structure (Hz)	21935	22823
Displacement caused by electrostatic force (mm)	2.56E-5	2.46E-5
Displacement caused by acceleration (mm)	1.07E-5	1.19E-5

Ring radius: 1 mm; ring width: 20 um; ring thickness: 250 um; Young’s modulus: 150 GPa; material density: 2300 kg/m<sup>3</sup>; applied electrostatic force: 5.43 μN; applied acceleration: 9.8 m/s<sup>2</sup>.

system is expressed as follows;

$$Z = \left| \frac{F}{X} \right| = |K - M\omega^2|. \tag{11}$$

The natural frequency of the structure is assumed to be  $\omega_1$ . The impedances of the two modes are,

$$\begin{aligned} Z_3 &= 0.105M\omega_1^2 \\ Z'_3 &= 0.53M\omega_1^2 \end{aligned} \tag{12}$$

Clearly,  $Z'_3$  is about five times  $Z_3$ . The authors believe that the natural vibration of the structure must be efficient. Thus, the mode associated with  $Z_3$  should be the desired mode of the rotating support rings.

The natural frequency of the structure is determined by adding the total kinetic energy and the total potential energy. The natural frequency of the structure,  $\omega$  is expressed as,

$$\omega \cong 1.048\omega_1. \tag{13}$$

This frequency is close to  $\omega_1$  and the mode is very similar to the second mode, and so the requirements are satisfied.

Table 2 compares the numerical and theoretical results, and the errors between these results are less than 5%. The part of the structure is modeled by quadrilateral shell elements, and the type of the element is Shell63. Fig. 8 indicates the convergence of the natural frequency with mesh refinement. The natural frequency of the second mode of the silicon structure is 22,823 Hz.

### 7. Sensitivity of sensor characteristics to the design specification, fabrication errors and theoretical errors

The sensitivity of the sensor characteristic to the design specification is obtained by calculating the natural frequency of the structure. Thereafter, many important system parameters can be derived and sensor performance can be estimated, for example, structural displacement and S/N ratio. The design parameters of this structure are the ring radius  $r$ ,

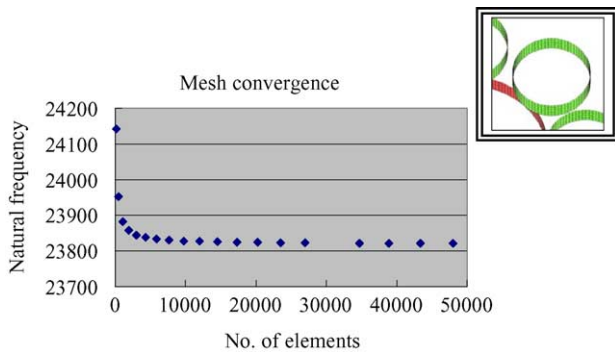


Fig. 8. Finite element analysis: the part of the structure modeled by quadrilateral shell elements and convergence of the natural frequency with mesh refinement.

Table 3  
Dimensions of parameters

	Symbol	Formula
Resonant frequency	$\omega_n$	$\sqrt{\frac{E}{\rho} \frac{w}{r^2}}$
Electrostatic force	$F_e$	$\varepsilon V^{cc2} \frac{r}{d^2}$
Coriolis force	$F_c$	$\Omega Q e \sqrt{\frac{\rho}{E}} \times V^{cc2} \frac{r^3}{wd^2}$
Rotation signal	$V_{rot}$	$\Omega Q e \frac{\sqrt{\rho}}{E \sqrt{E}} \times V^{cc3} \frac{r^6}{w^4 d^3}$
Acceleration signal	$V_{acc}$	$a \frac{\rho}{E} \times V^{cc} \frac{r^4}{dw^2}$
Signal to noise ratio for rotation	SNR(rot)	$\Omega Q e^2 \frac{1}{E} \times V^{cc3} \frac{r^3 t}{w^5 d^3}$
Signal to noise ratio for acceleration	SNR(acc)	$a e \sqrt{\frac{\rho}{E}} \times V^{cc} \frac{r^3 t}{d^2 w}$

$E$ : Young's modulus of material;  $\rho$ : material density;  $w$ : ring width;  $r$ : ring radius;  $\varepsilon$ : dielectric parameter;  $V^{cc}$ : static applied voltage;  $t$ : ring thickness;  $d$ : gap between ring and electrode;  $\Omega$ : rotation rate;  $Q$ : quality factor;  $a$ : acceleration.

the ring width  $w$  and the ring thickness  $t$ . Table 3 lists the results.

The radius, width and thickness of the ring and the width of the gap between the ring and the electrode may all manifest manufacturing errors. The sensitivities of sensor characteristics to the fabrication errors are estimated from the dimensional parameters, which are given in Table 3. Single crystal silicon is a suitable material, because its material properties, including density and Young's modulus, are stable. In fact, lithography seldom produces an erroneous radius of the ring. Hence, only an error in the width of the ring that arises during fabrication influences the resonant frequency. The ring width designed here is 10  $\mu\text{m}/20 \mu\text{m}$ , and the resultant errors are between 1 and 2  $\mu\text{m}$ , or 10%. The error in the width of the ring leads to an error in the width of the gap. The gap width used here is 2  $\mu\text{m}$ , so the error may strongly affect the performance of the sensor. The width of the gap increases as the width of the ring declines. An error in the width of the gap is the most common manufacturing error. Fig. 9 plots the normalized sensitivities, listed in Table 3, versus the change in the width of the gap. The width of the ring is designed to be ten times the width of the gap. The maximum error in the width of the gap is typically equal to the width of the designed gap, because of the etching process used in this work. The normalized sensitivities of the sensor's characteristics of interest to the inaccuracy in the width of the gap, as plotted in Fig. 9, imply that every such characteristic deteriorates as the width of the gap increases. In the worst case, parameters such as the S/N ratio decline to approximately one-fifth of their designed values. The anisotropy of the characteristics of the structure can cause coupling of the vibration modes, which is associated with the crystallographic orientation of the silicon wafer [31] and rotational misalignment during fabrication. Aligning the first mask with the crystals in the wafer can eliminate the anisotropy [32].

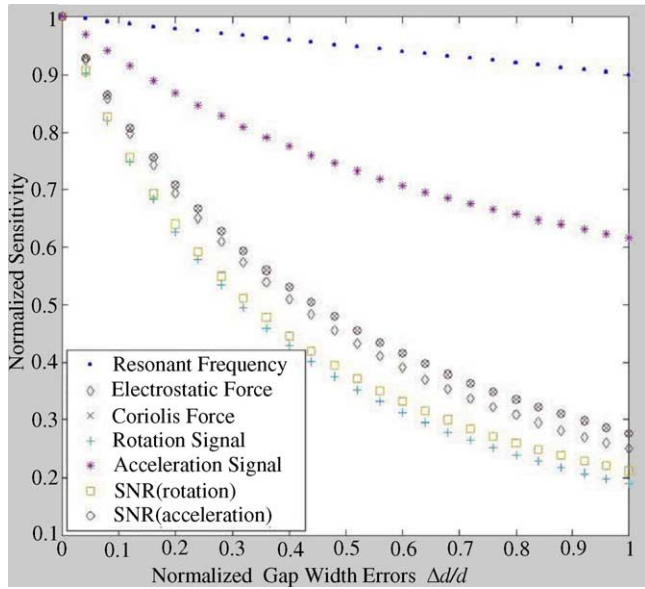


Fig. 9. Normalized sensitivities of sensor characteristics of interest to manufacturing errors in the gap width.

The sources of theoretical errors discussed herein include shifting of the natural frequency and angular acceleration. The structure is designed to vibrate at its resonant frequency, is close to the natural frequency if damping is weak. The factors that influence the resonant frequency must be considered. The first is damping. Providing a stable environment in which the sensor can operate is a solution. Acceleration is the second factor that influences the natural frequency. Theoretically, a force or acceleration causes the natural frequency to drift, governed by,

$$\Delta\omega = \omega_n \times \sqrt{\frac{r^2}{EIn^2\pi^2} \times F}. \quad (14)$$

According to the simulation results, this drift is neglect able. This effect depends on the ratio of the applied force to the relative stiffness of the structure. In this work, this ratio on the micro scale is too small to have any effect.

Eq. (7) specifies the errors due to the angular acceleration. As mentioned, the sensor incorporates designed rebalancing loops. A steady state error actually occurs in the rebalancing loops. This error is simply treated as a constant force applying to the structure. Eq. (7) for the second mode of vibration is solved as follows;

$$q_1 = \frac{1}{C} F_1 + \frac{B_2\dot{\Omega}}{C^2+KC+(B_2\dot{\Omega})^2} F_2 \quad (15)$$

$$q_2 = \frac{-B_2\dot{\Omega}}{C^2+KC+(B_2\dot{\Omega})^2} F_1 + \frac{C}{C^2+KC+(B_2\dot{\Omega})^2} F_2$$

When a force is applied, an angular acceleration causes the force in a single direction to have an unwanted influence in another direction, generating noise. Applying a sinusoidal force also creates this problem. Only increasing the effective stiffness and the gain of the rebalancing force can solve it.

An excessive effective stiffness makes the natural frequency extremely high, such that the circuit has a high working point. A better alternative is to increase the gain of the rebalancing force.

### 8. Fabrication and structural test

A process for fabricating the motion sensor and reducing the ARDE is developed [33], and described below. Fig. 10 displays a schematic view of the process described in the following sections, observed along AA' in Fig. 1. The process starts with a {1, 0, 0} n-type silicon wafer, which is patterned using photo resist, as depicted in Fig. 10(a). The patterned wafer is etched by silicon dry etching, as depicted in Fig. 10(b). A protective 500 Å thick layer of oxide is deposited following dry etching, as depicted in Fig. 10(c). This layer protects the structure during the subsequent etching of the backside, as revealed in Fig. 10(e). The 5000 Å thick interlayer of nickel is deposited on the glass wafer, as indicated in Fig. 10(d). This layer prevents the bonding of the glass to those areas that which should be removed during wet etching. It also prevents the structure from bonding to the glass, ensuring that the release of the structure is satisfactory. The silicon wafer and the glass wafer are bonded using an anodic bonder. The upper part of the resulting SOI structure is removed by back-sided wet etching, forming the structure depicted in Fig. 10(e). The areas designed to be removed are removed during this step. These areas are added to the design of the mask. The width of the line on the wafer is thus uniform, effectively reducing the aspect ratio-dependent effect during dry etching. The aforementioned protective layer guarantees the bonding from the silicon to the glass and resists the wet etching process. The structure is released by the wet etching of the glass wafer, as indicated in Fig. 10(f). Fig. 11 shows the resulting structure, with a thickness of 180 μm.

Fig. 12(a) presents the gap between the support ring and the electrode in their neutral positions. Fig. 12(b) indicates that the gap width is reduced when the electrode attracts the

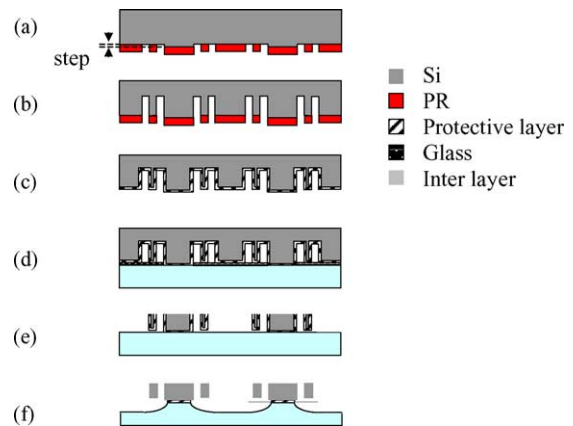


Fig. 10. Schematic view of fabrication process: (a) silicon patterning with photo resist; (b) deep silicon etching; (c) deposition of protective layer; (d) anodic bonding; (e) back-sided wet etching; and (f) release of structure.



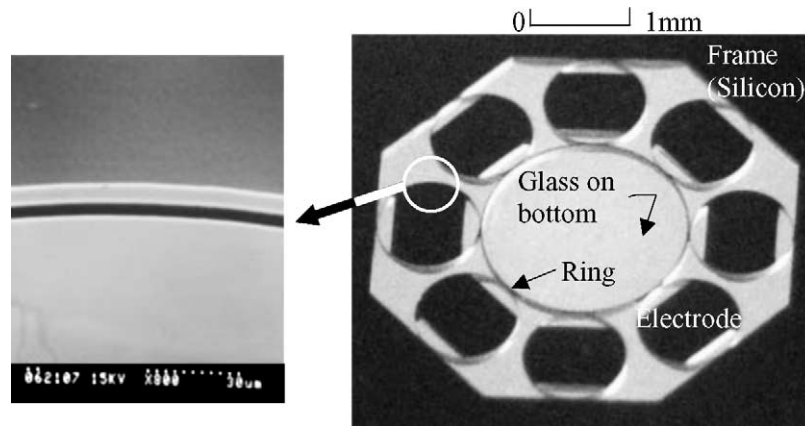


Fig. 11. Photographs of the ring-type motion sensor: top view of the structure with a height of 180  $\mu\text{m}$ , backlight through the glass and detailed view of structure of the gap between the ring and the electrode (SEM).

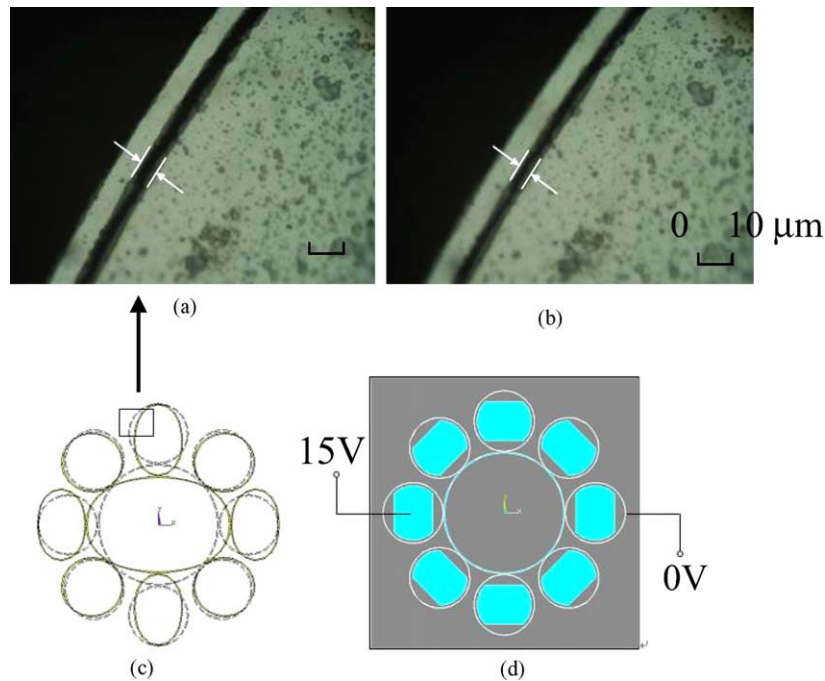


Fig. 12. (a) Photograph of the gap between the support and the electrode in their neutral positions; (b) photograph of the ring-type motion sensor when the electrode is attracting the support ring; (c) deformed structure; and (d) electrical connections.

support ring. Fig. 12(c) depicts the support ring is deformed into an oval shape. Fig. 12(d) depicts the electrical connection of the driving electrode. This deformed shape is very close to the designed mode of vibration. Due to the over-etching in dry etching process, the width of gap increases to 4  $\mu\text{m}$  and the natural frequency of the structure decreases to 19 kHz. This result follows the estimation of sensitivities.

## 9. Conclusion

This work presents a motion sensor that performs the functions of a gyroscope and an accelerometer. The capacitive

accelerometer and the vibrating ring gyroscope can be integrated in a motion sensor that detects both acceleration and rotation. The vibration of a circular ring can be theoretically decoupled into many modes, all of which exist simultaneously. The first mode stands for linear motion, while the second involves rotation. The detected signal can be output simply and clearly by adding rebalancing control loops and designing a structure with relatively high stiffness. The rotational symmetry of the structure enables the sensor to detect rotation. The mirror symmetry maintains the performance of the sensor under acceleration. Rebalancing loops enhance the sensor as both a gyroscope and an accelerometer. A lack of both rotational symmetry and mirror symmetry

causes the detected signal to contain much noise. The process of estimating the natural frequency is to separate the structure into three parts; to determine the natural frequency of each part individually, and then to calculate the composite natural frequency of the structure. Two simple concepts are applied to determine the exact natural frequency of the structure. The errors between the numerical and the theoretical results are less than 5%, and the modes of vibration are exactly as required. The error in the gap width is the major concern regarding the fabrication of the structure presented herein. Every considered characteristic deteriorates as the width of the gap increases. In the worst case, parameters such as the S/N ratio fall to approximately one-fifth of the designed values. Structural testing demonstrates that the deformed shape of the structure and its driving frequency are very close to those of the designed mode of vibration. Based on those design considerations, the vibrating ring-type motion sensor can be used to integrate the functions of a gyroscope and an accelerometer.

### Acknowledgement

The authors would like to thank the National Science Council of the Republic of China, Taiwan, for financially supporting this research under Contract No. NSC89-2212-E-009-062.

### References

- [1] L.K. Baxter, *Capacitive Sensors Design and Applications*, IEEE Press, New York, 1997.
- [2] A. Lawrence, *Modern Inertial Technology Navigation Guidance and Control*, New York, Springer-Verlag, 1993.
- [3] W.H. Quick, Theory of the vibrating string as an angular motion sensor, *Trans. ASME, J. Appl. Mech.* 31 (1964) 523–534.
- [4] W.D. Gates, Vibrating angular rate sensors may threaten the gyroscope, *Electronics* 10 (1968) 130–134.
- [5] D. Boocock, L. Maunder, Vibration of a symmetry tuning fork, *J. Mech. Eng. Sci.* 11 (4.) (1969).
- [6] L. Parameswaran, C. Hsu, M.A. Schmidt, A merged MEMS-CMOS process using silicon wafer bonding, in: *Proceedings of the IEEE International Electron Devices Meeting*, Washington, DC, December 1995.
- [7] P. Greiff, B. Boxenhorn, T. King, L. Niles, Silicon monolithic micromechanical gyroscope, in: *Proceedings of the 6th International Conference on Solid-State Sensors and Actuators (Transducers'91)*, San Francisco, CA, June 1991, pp. 966–968.
- [8] W.A. Clark, R.T. Howe, R. Horowitz, Surface micromachined-axis vibratory rate gyroscope, in: *Proceedings of the Tech. Dig. Solid-State Sensor and Actuator Workshop*, Hilton Head Island, SC, June 1996, pp. 283–287.
- [9] T. Juneau, A.P. Pisano, Micromachined dual input axis angular rate sensor, in: *Proceedings of the Tech. Dig. Solid-State Sensor and Actuator Workshop*, Hilton Head Island, SC, June 1996, pp. 299–302.
- [10] W. Geiger, B. Folkmer, J. Merz, H. Sandmaier, W. Lang, A new silicon rate gyroscope, in: *Proceedings of the IEEE Micro Electro Mechanical Systems Workshop (MEMS'98)*, Heidelberg, Germany, February 1998, pp. 615–620.
- [11] T. Juneau, A.P. Pisano, J.H. Smith, Dual axis operation of a micro-machined rate gyroscope, in: *Proceedings of the Tech. Dig. 9th International Conference on Solid-State Sensors and Actuators (Transducers'97)*, Chicago, IL, June 1997, pp. 883–886.
- [12] M.W. Putty, K. Najafi, A micromachined vibrating ring gyroscope, in: *Proceedings of the Tech. Dig. Solid-State Sensor and Actuator Workshop*, Hilton Head Island, SC, June 1994, pp. 213–220.
- [13] F. Gretillat, M.-A. Gretillat, N.F. de Rooij, Improved design of a silicon micromachined gyroscope with piezoresistive detection and electromagnetic excitation, *IEEE J. Microelectromech. Syst.* 8 (3) (1999) 243–250.
- [14] D.R. Sparks, S.R. Zarabadi, J.D. Johnson, Q. Jiang, M. Chia, O. Larsen, W. Higdon, P. Castillo-Borelley, A CMOS integrated surface micromachined angular rate sensor: its automotive applications, in: *Proceedings of the Tech. Dig. 9th Int. Conf. Solid-State Sensors and Actuators (Transducers'97)*, Chicago, IL, June 1997, pp. 851–854.
- [15] F. Ayazi, K. Najafi, A HARPSS polysilicon vibrating ring gyroscope, *IEEE J. Microelectromech. Syst.* 10 (2) (2001) 169–179.
- [16] A. Selvakumar, K. Najafi, High density vertical comb array microactuators fabricated using a novel bulk/poly-silicon trench refill technology, in: *Proceedings of the Tech. Dig. Solid-State Sensor and Actuator Workshop*, Hilton Head Island, SC, USA, 1994, pp. 138–141.
- [17] J.S. Burdess, T. Wren, The theory of a piezoelectric disc gyroscope, *IEEE Trans. Aerospace Electron. Syst.* 22 (4) (1986) 411–418.
- [18] B.J. Gallacher, J.S. Burdess, A.J. Harris, Principles of a three-axis vibrating gyroscope, *IEEE Trans. Aerospace Electron. Syst.* 37 (4) (2001) 1333–1343.
- [19] E.J. Loper, D.D. Lynch, Projected system performance based on recent HRG test results, in: *Proceedings of the 5th Digital Avionics System Conference*, Seattle, Washington, November 1983.
- [20] L.M. Roylance, J.B. Angeel, A batch-fabricated silicon accelerometer, *IEEE Trans. Electron. Devices* 26 (12) (1979) 1911–1917.
- [21] H. Seidel, H. Riedel, R. Jolbeck, G. Muck, W. Kuoke, M. Koniger, Capacitive silicon accelerometer with highly symmetrical design, *Sens. Actuators A21–A23* (1990) 312–315.
- [22] K. Okada, Tri-axial piezo-electric accelerometer, in: *Proceedings of Transducer'95*, 25–29 June 1995, pp. 566–569.
- [23] B. Puers, L. Reynaret, W. Soneyw, W.M.C. Sansen, A new uniaxial accelerometer in silicon based on the piezo-junction effect, *IEEE Trans. Electron. Devices* 35 (8) (1988) 764–770.
- [24] R. Hiratsuka, D.C.V. Duyn, T. Otaredain, P. de Vries, Design consideration for the thermal accelerometer, *Sens. Actuators A32* (1992) 380–385.
- [25] E. Abbaspour-Sani, R.S. Huang, C.Y. Kwok, A linear electromagnetic accelerometer, *Sens. Actuators A44* (1994) 103–109.
- [26] C.-H. Liu, T.W. Kenny, A high-precision, wide-bandwidth micromachined tunneling accelerometer, *IEEE J. Microelectromech. Syst.* 10 (3) (2001) 425–433.
- [27] H. Bruschi, G. Torzo, Method for accurate resonant frequency measurement with a phase modulated feedback loop, *Rev. Sci. Instrum.* 58 (1978) 2181–2184.
- [28] S. Timoshenko, D.H. Young, W. Weaver J.R., *Vibration Problems in Engineering*, fourth ed., John Wiley & Sons, 1974.
- [29] G.H. Duffey, *Applied Group Theory for Physicists and Chemists*, Prentice-Hall, Englewood Cliffs, 1992.
- [30] W. Soedel, *Vibrations of Shells and Plates*, Marcel Dekker, New York, Basel, 1981.
- [31] R. Eley, C.H.J. Fox, S. McWilliam, Anisotropy effects on the vibration of circular rings made from crystalline silicon, *J. Sound Vib.* 228 (1) (1999) 11–35.
- [32] J.M. Lai, W.H. Chieng, Y-C. Huang, Precision alignment of mask etching with respect to crystal orientation, *J. Micromech. Microeng.* 8 (4) (1998) 327–329.
- [33] J.H. Weng, W.H. Chieng, J.M. Lai, Structural fabrication of a ring-type motion sensor, *J. Micromech. Microeng.* 14 (5) (2004) 710–716.

## Biographies

*Professor Wei-Hua Chieng* received a PhD in mechanical engineering at Columbia University in 1989. He has been a full professor in mechanical engineering at National Chiao-Tung University since 1996 and was appointed associated professor in 1989. His current research is in MEMS and electrical circuit design.

*Mr. Jui-Hong Weng* received BS and MS degrees in mechanical engineering at National Chiao-Tung University, Taiwan, in 1996 and

1998, respectively. He has been a PhD candidate in mechanical engineering at National Chiao-Tung University, Taiwan, since 2000. From 1998, he is researching on MEMS. His current research is micromachined gyroscope and accelerometer.

*Dr. Jenn-Min Lai* received a PhD in mechanical engineering department of National Chiao-Tung University, Taiwan, in 1999. Since 2000, he has been a senior engineer of R&D Center in NeoStones Micro-Fabrication Corporation. He is in charge of process development of MEMS.